

Obscuration properties of mid-IR selected AGN

G. Mountrichas¹, I. Georgantopoulos¹, A. Ruiz¹, G. Kampylis^{1,2}

¹National Observatory of Athens, V. Paulou & I. Metaxa, 15236, Greece

²Department of Physics, University of Patras, Patras, Greece

17 March 2022

ABSTRACT

The goal of this work is to study the obscuration properties of mid-infrared (mid-IR) selected AGN. For that purpose, we use *WISE* sources in the Stripe 82-XMM area to identify mid-IR AGN candidates, applying the Assef et al. criteria. Stripe 82 has optical photometry ≈ 2 times deeper than any single-epoch SDSS region. XMM-Newton observations cover $\sim 26 \text{ deg}^2$. Applying the aforementioned criteria, 1946 IR AGN are selected. $\sim 78\%$ have SDSS detection, while 1/3 of them is detected in X-rays, at a flux limit of $\sim 5 \times 10^{-15} \text{ erg s}^{-1} \text{ cm}^{-2}$. Our final sample consists of 507 IR AGN with X-ray detection and optical spectra. Applying a $r - W2 > 6$ colour criterion, we find that the fraction of optically red AGN drops from 43% for those sources with SDSS detection to 23% for sources that also have X-ray detection. X-ray spectral fitting reveals 40 ($\sim 8\%$) X-ray absorbed AGN ($N_H > 10^{22} \text{ cm}^{-2}$). Among the X-ray unabsorbed AGN, there are 70 red systems. To further investigate the absorption of these sources, we construct Spectral Energy Distributions (SEDs) for the total IR AGN sample. SED fitting reveals that $\sim 20\%$ of the optically red sources have such colours because the galaxy emission is a primary component in the optical part of the SED, even though the AGN emission is not absorbed at these wavelengths. SED fitting also confirms that 12% of the X-ray unabsorbed, IR AGN are optically obscured.

Key words: Galaxies: active, Galaxies: evolution, Galaxies: nuclei, X-rays: galaxies

1 INTRODUCTION

Mid-infrared (mid-IR) surveys have been proven extremely capable of detecting Active Galactic Nuclei (AGN), since they are affected less by extinction. The material that obscures AGN even at X-ray energies, is heated by the AGN and re-emits the nuclear radiation at infrared (IR) wavelengths. Thus, mid-IR surveys trace obscured sources missed even by hard X-ray surveys (e.g., Georgantopoulos et al. 2008; Fiore et al. 2009). *Spitzer* was the first IR mission used to demonstrate the efficiency of selecting AGN from a mid-IR dataset, by applying colour-selection techniques (e.g., Stern et al. 2005; Donley et al. 2012). These techniques have now been adapted and used for the *Wise-field Infrared Survey Explorer* (*WISE*; Wright et al. 2010).

WISE completed an all-sky coverage in four mid-IR bands 3.4, 4.6, 12 and $12 \mu\text{m}$ (W1, W2, W3 and W4 bands, respectively). Several colour regions have been defined that efficiently identify AGN, in particular at high luminosities. For example, Mateos et al. (2012) suggested a selection method using three *WISE* colours. Stern et al. (2012) used the W1 and W2 bands and applied a simple $W1 - W2 \geq 0.8$ criterion to reliably select AGN with $W2 < 15.05$ in the COSMOS field. Assef et al. (2013) extended the aforementioned criterion and provided a selection of AGN for fainter *WISE* sources.

Previous studies have shown that a fraction of these IR se-

lected AGN are missed by X-rays. This is attributed to their heavy obscuration in the X-ray band. Del Moro et al. (2016) studied a sample of 33 mid-IR selected quasars with intrinsic luminosity $\nu L_{6\mu\text{m}} > 6 \times 10^{44} \text{ erg s}^{-1}$ at redshift $z \approx 1 - 3$. Despite their high IR luminosity, $\sim 30\%$ of the sources, i.e. nine quasars, are undetected in X-rays. Among the X-ray detected IR sources, 16 out of 24 ($\sim 70\%$) are heavily obscured ($N_H > 2 \times 10^{23} \text{ cm}^{-2}$). Mateos et al. (2017) used 199 X-ray selected AGN from the Bright Ultra-hard XMM-Newton Survey (BUXS) and found a substantial population of X-ray undetected sources with high-covering factor tori. They claim that the majority of luminous AGN live in highly obscured environments that remain undetected in X-rays at the depths of $< 10 \text{ keV}$ wide-area surveys. Mendez et al. (2013) found that the percentage of IR AGN that are also detected in X-rays, varies significantly (47% to 90%) depending on the depth of the X-ray and IR surveys (see their Fig. 8). Increasing the depth of the IR data reduces the fraction of X-ray detected sources, while increasing the depth of the X-ray data increases the fraction of X-ray detections.

Secrest et al. (2015) applied the Mateos et al. (2012) colour selection criteria on the *WISE* sample and created a sample of 1.4 million AGN candidates. Mountrichas et al. (2017) used this catalogue to explore the X-ray properties of mid-IR selected AGN. In this work they study only the most luminous of these sources ($\log(\nu L_\nu / \text{erg s}^{-1}) \geq 46.2$). Specifically, they cross-correlated the Secrest et al. (2015) catalogue with the subsample of the

3XMM X-ray dataset with available X-ray spectra (Corral et al. 2015) and optical spectroscopy from SDSS/BOSS (Alam et al. 2015). Due to the requirement for optical (SDSS) identifications, their sample is biased towards type-1 sources. Their analysis revealed seven obscured AGN in X-rays. However, none of them was absorbed based on their optical continuum.

LaMassa et al. (2019) studied the demographics of AGN in Stripe82X (LaMassa et al. 2013a,b). They compiled a catalogue of 4847 AGN, based on their X-ray luminosities or *WISE* colours. Stripe 82X has dedicated SDSS observations, therefore their sample does not suffer from the optical spectroscopic limitations of the Mountrichas et al. (2017) dataset. Their analysis showed that 61% of X-ray AGN are not selected as mid-IR AGN, while 22% of X-ray sources have no *WISE* detection. Moreover, 58% of *WISE* AGN are not detected in X-rays. However, based on the $W1 - W2$ colour difference, sources undetected in X-rays do not appear to be redder than those detected in X-rays. Previous studies have shown, that although X-ray selection is able to identify even very inactive AGN, the X-ray emission is easily absorbed by gas. Especially, at the softer, 10 KeV energies probed by the Chandra and XMM satellites. On the other hand, mid-IR selection is less susceptible to absorption, but only identifies high luminosity AGN, i.e., those systems that the AGN outshines the stellar emission from the galaxy (e.g., Barmby et al. 2006; Georgantopoulos et al. 2008; Eckart et al. 2010).

In this work, we use *WISE* sources in the Stripe 82X survey (LaMassa et al. 2015; LaMassa et al. 2019) and apply the colour criteria of Stern et al. (2012), modified by Assef et al. (2013) to select mid-IR AGN candidates. First, we derive the obscuration properties using the optical/mid-IR colours and Spectral Energy Distributions (SED). Second, we use only those sources with X-ray detection. Our goal is to study the X-ray properties of these mid-IR selected AGN, by fitting their X-ray spectra. We also compare the X-ray with the optical colour of these sources.

2 DATA

2.1 Sample selection

Stripe 82 covers an area of $\sim 300 \text{ deg}^2$ on the celestial equator and has been repeatedly scanned by the SDSS. In addition the field has been partially covered by observations at other wavelengths, e.g., UKIDSS (Lawrence et al. 2007) and *Herschel* (Viero et al. 2014). The Stripe 82X survey (LaMassa et al. 2013a,b, 2015) covers $\sim 31 \text{ deg}^2$ on the sky and was designed to take advantage of the wealth of multi-wavelength information provided by Stripe 82. Its goal is to reveal high luminosity AGN at high redshifts.

Stripe 82X has both Chandra and XMM-*Newton* observations. In this work we study the X-ray spectral properties of IR selected AGN and compare them with their optical colours and SEDs. For that purpose we require 3XMM observations (Stripe 82-XMM). About half of the Stripe 82-XMM survey (15.6 deg^2) is contiguous and reaches an $0.5 - 10 \text{ keV}$ flux limit of $\sim 10^{-14} \text{ erg s}^{-1} \text{ cm}^{-2}$ at half survey area. The median exposure time is $\sim 6 \text{ ks}$, while the coadded depth in the overlapping regions reaches $\sim 6 - 8 \text{ ks}$ (LaMassa et al. 2019). The remaining 10.6 deg^2 , comprise of 4.6 deg^2 of proprietary XMM-*Newton* data, with exposure time of $4 - 5 \text{ ks}$ (12 ks in regions with greatest overlap) and 6 deg^2 of archival data (LaMassa et al. 2013).

We use $\sim 300,000$ *WISE* sources in the Stripe 82-XMM area to select mid-IR AGN. We apply the criteria presented in Stern et al.

(2012) combined with the modified selection criterion described in Assef et al. (2013), for fainter *WISE* sources. Specifically, the selection criteria we apply are:

For $W2 < 15.05$

$$W1 - W2 \geq 0.8, \quad (1)$$

and for $15.05 \leq W2 \leq 17.11$

$$W1 - W2 > a_R \exp [\beta_R (W2 - \gamma_R)^2], \quad W1_{\text{snr}} > 3, \quad (2)$$

where $W1, W2$ are the *WISE* photometric bands, at 3.4 and $4.6 \mu\text{m}$, $W1_{\text{snr}}$ is the S/N ratio of the $W1$ band and $(a_R, \beta_R, \gamma_R) = (0.662, 0.232, 13.93)$, to select AGN at a 90% reliability. We find 1946 IR AGN that lie within the 3XMM footprint. 1507 of these sources have optical (SDSS DR13; Albareti et al. 2017) counterpart and 824 have available optical spectrum. We cross-match these sources with the 499, 266 X-ray sources of the 3XMM-DR7 catalogue (Rosen et al. 2016). For the cross-match we use TOPCAT, version 4.6, using a radius of 3 arcsec. 0.2% spurious sources are expected among common sources between the two datasets (Mountrichas et al. 2017). The number of sources in each subsample is presented in Table 1. 1250 (1946-696), i.e., $\sim 64\%$, of the IR selected AGN are undetected in X-rays. This percentage is in agreement with the 58% found in LaMassa et al. (2019).

2.2 Sample properties

The scope of the paper is to study the X-ray absorption of IR selected AGN and compare it with optical/mid-IR criteria. Therefore, both X-ray and optical identification are needed for the sources. However, this requirement imposes selection biases in the AGN sample. In the following, we study the impact of these biases on our X-ray sample.

Previous studies have found a correlation between the optical colour and the X-ray obscuration (e.g., Civano et al. 2012). Yan et al. (2013) showed that type-2 AGN candidates at $z \leq 3$, can be identified by applying the following colour criteria: *WISE* $W1 - W2 > 0.8, W2 < 15.2$ combined with $r - W2 > 6$ (Vega). In Fig. 1 (left panel) we plot the $r - W2$ distributions of the AGN samples. Sources with only SDSS detection, show a peak in their distribution at $r - W2 \approx 5.5$. However, a second peak is present at larger $r - W2$ values (≈ 8.5). When an SDSS spectrum requirement is applied, this second peak is not detected. However, we notice a wide tail at high $r - W2$ values. Our X-ray detected sources completely miss this optically, possibly obscured AGN population. These distributions are quantified in Table 2, that presents the fraction of optically red sources in the various subsamples. Based on the $r - W2$ distributions, we notice that $r - W2 = 7$ cut seems more natural, since it separates two peaks. Given the prevalence of the $r - W2 = 6$ cut in the literature, we keep the latter cut in our analysis. However, in Table 2 we also present the fraction of optically red sources, using the $r - W2 = 7$ cut. Regardless of the exact value of the optical/mid-IR cut applied, the measurements confirm our aforementioned findings, i.e., IR selected AGN that are undetected by X-rays are probably preferentially redder than those detected in X-rays (but see Fig. 16 in LaMassa et al. 2019). Middle and right panels of Fig. 1, present the i -band and redshift distributions of the AGN samples. We notice that X-ray detected sources are brighter than $i \lesssim 22$.

Mateos et al. (2012) used MIR *WISE* colours to select luminous AGN candidates. Using these AGN, they defined a highly complete, mid-IR colour wedge that their sources occupy. X-ray

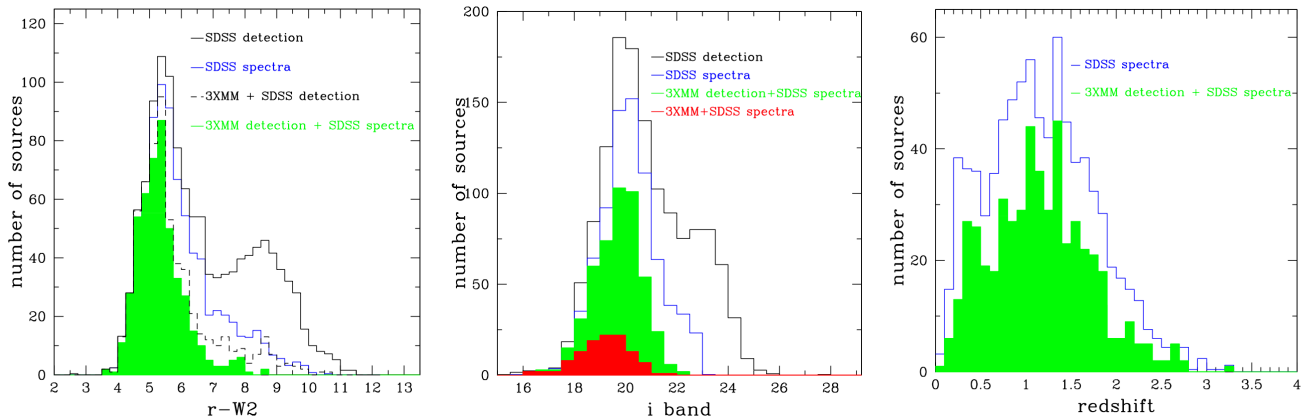


Figure 1. From left to right: $r - W2$, i -band and redshift distributions of the AGN samples.

Table 1. The number of mid-IR selected AGN in Stripe 82X, with optical/X-ray counterparts and spectra.

Mid-IR selected AGN	1946
3XMM detection	696
SDSS detection	1507
SDSS spectra	824
3XMM and SDSS detection	646
3XMM detection + SDSS spectra	507

Table 2. Fraction of optically red sources found in our IR selected AGN in Stripe 82X. In the parentheses we quote the total number of AGN in each subsample.

sample	red sources	red sources
	$r - W2 > 6$	$r - W2 > 7$
SDSS detection (1507)	43%	30%
SDSS spectra (824)	31%	13%
3XMM+SDSS detection (646)	23%	9%
3XMM detection + SDSS spectra (507)	20%	6%

detected AGN reside in the lower part of this wedge (see their Figures 2 and 6). In Fig. 2.2 we plot $W1-W2$ versus $W2-W3$ colours, for those of our sources with $W3_{snr} > 5$. In agreement with Mateos et al. (2012), our X-ray detected AGN occupy the lower part of the mid-IR colour diagram. However, optically red sources ($r - W2 > 6$, red points in Fig. 2.2) seem to be randomly distributed in the colour diagram.

Table 3. The mean values of N_H and Γ for the X-ray sample as well as for various subsamples, based on the number of source photons. The errors correspond to the mean values of the 1σ uncertainties of the measurements.

sample	no. of sources	$\log(N_H/\text{cm}^{-2})$	Γ
All sources	507	20.6 ± 0.6	1.96 ± 0.20
< 50 counts	152	20.9 ± 0.9	1.93 ± 0.28
< 100 counts	250	20.9 ± 0.8	1.93 ± 0.25
> 100 counts	257	20.3 ± 0.4	1.99 ± 0.17
> 500 counts	40	20.2 ± 0.3	2.05 ± 0.09

3 X-RAY AND OPTICAL ABSORPTION OF IR AGN

In this Section, we study the X-ray absorption of the 507 IR selected AGN with X-ray detection and optical spectra. We then compare the X-ray with the optical absorption (e.g., Glikman et al. 2018), using optical/mid-IR colours and SED fitting.

To study the X-ray properties of the IR selected AGN, we use Xspec v12.8 (Arnaud 1996). Photoelectric absorption is included in all the spectral models (wabs, in XSPEC notation), fixed at the Galactic value at the source coordinates given by Leiden/Argentine/Bonn (LAB) Survey of the Galactic HI (Kalberla et al. 2005). A single power-law model absorbed by neutral material surrounding the central source is applied on the X-ray spectra. For that purpose, we used the fitting and modelling software Sherpa (version 4.9.1; Freeman et al. 2001). We followed the Bayesian technique proposed in Buchner et al. (2014), using the analysis software BXA (Bayesian X-ray Analysis), that connects the nested sampling algorithm MultiNest (Feroz et al. 2009) with Sherpa. A nested sampling algorithm allows a full exploitation of the parameter space, avoiding solutions that correspond to local minima which is a common problem with standard minimization techniques (e.g. the Levenberg-Marquardt algorithm). In the BXA framework, a probability prior is assigned to each free parameter of the model. For the power law, photon index, Γ , we used a gaussian prior with mean value 1.9 and standard deviation 0.15 (Nandra & Pounds 1994). For the remaining parameters, we used flat, uninformative priors. Our spectral fits, follow the same procedure to build the XMMFITCAT-z (see Ruiz et al., in prep., <http://xraygroup.astro.noa.gr/Webpage-prodex/>).

The mean N_H and Γ values of the sample are $N_H = 10^{20.6 \pm 0.6} \text{ cm}^{-2}$ and $\Gamma = 1.96 \pm 0.20$. The quoted errors correspond to the mean values of the 1σ uncertainties. We also split the sample into various subsamples, based on the number of source photons. The mean values of N_H and Γ are presented in Table 3. Fig. 3 presents the distributions of N_H (left panel) and Γ (right panel) values. Our analysis reveals 40 sources ($\sim 8\%$) that have $N_H > 10^{22} \text{ cm}^{-2}$. This number increases to 65 ($\sim 13\%$) if we loosen our X-ray absorption criterion, i.e., $N_H > 10^{21.5} \text{ cm}^{-2}$. However, we note that our X-ray spectra extend to energies up to 10 keV. Modelling X-ray spectra at higher energies could possibly change the estimated N_H values (Civano et al. 2015).

Optical/mid-IR colour criteria reveal that 18/40 (45%) of the X-ray absorbed AGN are also optically red ($r - W2 > 6$). This percentage is higher compared to the fraction of red sources among

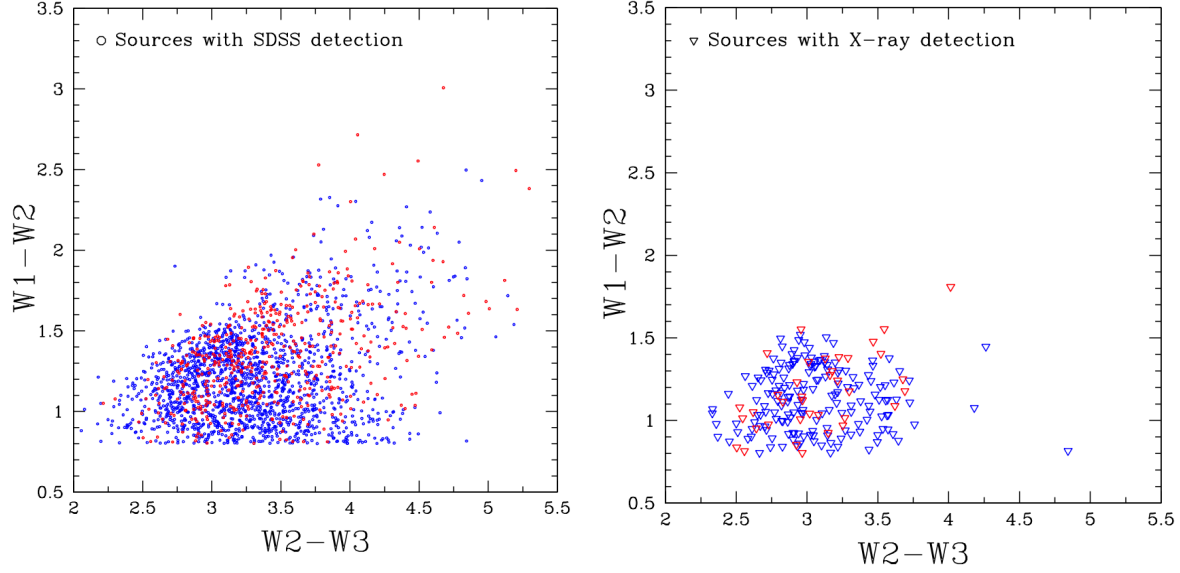


Figure 2. W1-W2 vs. W2-W3 of those sources with SDSS detection (left panel) and those with X-ray detection (right panel). Sources with $W3_{\text{snr}} < 5$ have been excluded. Optically blue sources ($r\text{-}W2 < 6$) are shown in blue. Optically red sources are shown in red ($r\text{-}W2 > 6$).

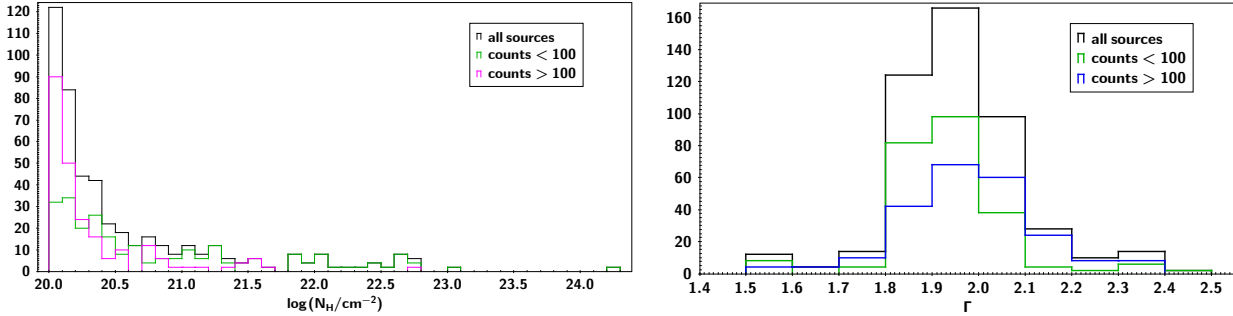


Figure 3. The distribution of N_H (left panel) and Γ (right panel) values of the 507 IR AGN with X-ray detection (black line), using spectral fitting. The green line presents the distributions of those sources with less than 100 photon counts and the blue line the distributions of those sources with more than 100 counts.

the 507 sources (20%, see Table 2). However, among the non X-ray absorbed sources (467), there are 70 (15%) optically red AGN (Fig. 4). Prompted by this, we construct SEDs for the sample of the 507 AGN and further examine their obscuration (for more details see Appendix). The SED fitting analysis reveals that 86% of the red objects are optically obscured, based on the estimated inclination angle of the torus. Thus, there is a very good agreement between the optical colours and the SEDs of the sources. All 18 IR AGN that are X-ray absorbed and optically red are also obscured based on their SEDs. An example of the X-ray spectrum and the SED of one of these sources is presented in Fig. 5. Among the 70 optically red AGN that are not X-ray absorbed, 58 (83%) are obscured, based on their SEDs (Fig. 6). The $r - W2$ values and the X-ray spectral results of these sources are presented in Table 4. As can be seen in this Table, there are a few sources that present some X-ray obscuration, but do not meet our X-ray obscuration criterion, i.e., their N_H value is ($10^{21.5} < N_H < 10^{22}$) cm^{-2} . However, a large number of sources that have high number of counts (a few hundred up to a couple of thousand) present no indication of X-ray obscuration ($N_H < 10^{20.5-21}$ cm^{-2}). For the remaining 12 sources (17%) the SEDs reveal they are galaxy dominated systems, i.e., the galaxy emission is a primary component of the SED

in the optical part of the spectrum, even though the AGN emission is not absorbed at these wavelengths (Fig. 7). The aforementioned numbers do not change if we lower our X-ray absorption criterion, i.e. $N_H > 10^{21.5}$ cm^{-2} . We conclude, the SED fitting analysis confirms that there is a fraction ($\frac{58}{467} \approx 12\%$) of IR AGN that are red, obscured sources without presenting X-ray absorption.

In Fig. 8 we plot the redshift, SFR, stellar mass (derived by SED fitting) and X-ray luminosity (derived by X-ray spectral fitting) distributions (blue shaded regions) of these 58 systems and compare them with the total population of X-ray unabsorbed, IR AGN. The plots indicate that these sources are X-ray luminous AGN that reside in massive systems ($\log(M_*/M_\odot) > 10.5$).

4 SUMMARY

We use the $\sim 300,000$ sources of the Stripe 82-XMM area to select mid-IR AGN by applying the selection criteria presented in Stern et al. (2012) combined with those described in Assef et al. (2013) for fainter sources (LaMassa et al. 2019). The sample consists of 1946 AGN candidates, with 90% reliability. For 1507 sources there are SDSS magnitudes available. Their optical/mid-IR colours $r -$

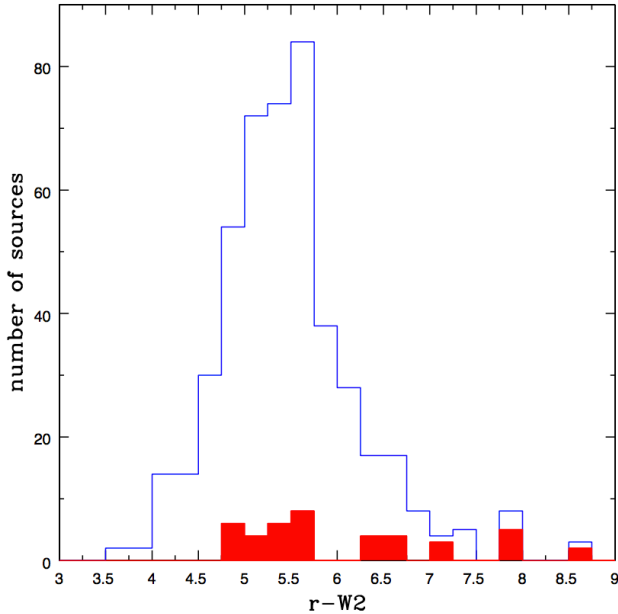


Figure 4. $r - W2$ distributions of the 507 IR AGN with X-ray detection (blue line) and the 40/507 that are X-ray absorbed (red shaded region).

$W2 > 6$ (Yan et al. 2013), suggest that about 40% of the sample is obscured. We use SED fitting to further investigate the optical obscuration of these sources, using the inclination angle as a proxy of the optical obscuration. The SED analysis corroborates that these sources are obscured.

507 IR AGN are detected in X-rays and have also optical spectra available. We examine the biases the aforementioned requirements impose on our final AGN sample. Our findings reveal that there is a (significant) population of red sources that are excluded when we require optical spectra and X-ray detection. Specifically, the percentage of red sources with SDSS detection drops from 43% to 20% when X-ray detection and optical spectra are required (Table 2). Therefore, the sample used in our X-ray analysis is biased against the redder sources. The X-ray spectral fitting analysis suggests that 8% of the sources have column densities $N_H > 10^{22} \text{ cm}^{-2}$. There are 70 (15% of the sample) optically red AGN, that are X-ray unabsorbed. SEDs confirmed that 58/70 (83%) of them are obscured sources. The remaining are galaxy dominated systems, i.e., the galaxy emission is a primary component of the SED in the optical part of the spectrum, even though the AGN emission is not absorbed. Therefore, our analysis shows that: (i) The IR acted AGN sample contains a significant fraction of optically red sources (ii) when we consider IR selected AGN that are also X-ray detected, our results reveal that these sources are preferentially associated with unobscured systems.

5 ACKNOWLEDGMENTS

The authors are grateful to the anonymous referee for helpful comments. GM and AR acknowledge support of this work by the PROTEAS II project (MIS 5002515), which is implemented under the "Reinforcement of the Research and Innovation Infrastructure" action, funded by the "Competitiveness, Entrepreneurship and Innovation" operational programme (NSRF 2014-2020)

and co-financed by Greece and the European Union (European Regional Development Fund).

This research has made use of data obtained from the 3XMM XMM-Newton serendipitous source catalogue compiled by the 10 institutes of the XMM-Newton Survey Science Centre selected by ESA.

This work is based on observations made with XMM-Newton, an ESA science mission with instruments and contributions directly funded by ESA Member States and NASA.

Funding for the Sloan Digital Sky Survey IV has been provided by the Alfred P. Sloan Foundation, the U.S. Department of Energy Office of Science, and the Participating Institutions. SDSS-IV acknowledges support and resources from the Center for High-Performance Computing at the University of Utah. The SDSS web site is www.sdss.org.

SDSS-IV is managed by the Astrophysical Research Consortium for the Participating Institutions of the SDSS Collaboration including the Brazilian Participation Group, the Carnegie Institution for Science, Carnegie Mellon University, the Chilean Participation Group, the French Participation Group, Harvard-Smithsonian Center for Astrophysics, Instituto de Astrofísica de Canarias, The Johns Hopkins University, Kavli Institute for the Physics and Mathematics of the Universe (IPMU) / University of Tokyo, Lawrence Berkeley National Laboratory, Leibniz Institut für Astrophysik Potsdam (AIP), Max-Planck-Institut für Astronomie (MPIA Heidelberg), Max-Planck-Institut für Astrophysik (MPA Garching), Max-Planck-Institut für Extraterrestrische Physik (MPE), National Astronomical Observatories of China, New Mexico State University, New York University, University of Notre Dame, Observatório Nacional / MCTI, The Ohio State University, Pennsylvania State University, Shanghai Astronomical Observatory, United Kingdom Participation Group, Universidad Nacional Autónoma de México, University of Arizona, University of Colorado Boulder, University of Oxford, University of Portsmouth, University of Utah, University of Virginia, University of Washington, University of Wisconsin, Vanderbilt University, and Yale University.

REFERENCES

- Alam S., et al., 2015, APJS, 219, 12
- Albareti F. D., Comparat J., Gutiérrez C. M., Prada F., Pâris I., Schlegel D., López-Corredoira M., Schneider D. P., Manchado A., García-Hernández D. A., Petitjean P., Ge J., 2015, MNRAS, 452, 4153
- Albareti F. D., et al., 2017, ApJS, 233, 25
- Arnaud K. A., 1996, ASPC, 101, 17
- Assef R. J., et al., 2013, ApJ, 772, 26
- Barmby P., Alonso-Herrero A., Donley J. L., Egami E., Fazio G. G., Georgakakis A., Huang J.-S., Laird E. S., Miyazaki S., Nandra K., Park S. Q., Pérez-González P. G., Rieke G. H., Rigby J. R., Willner S. P., 2006, ApJ, 642, 126
- Bruzual G., Charlot S., 2003, MNRAS, 344, 1000
- Buchner J., et al., 2014, A&A, 564, 125
- Calzetti D., Armus L., Bohlin R. C., Kinney A. L., Koornneef J., Storchi-Bergmann T., 2000, ApJ, 533, 682
- Ciesla L., et al., 2015, A&A, 576, 19
- Civano F., Elvis M., Brusa M., Comastri A., Salvato M., Zamorani G., Aldcroft T., Bongiorno A., Capak P., Cappelluti N., Cisternas M., Fiore F., Fruscione A., Hao H., Kartaltepe J., Koekemoer A., Gilli R., Impey C. D., Lanzuisi G., Lusso E., Mainieri V., Miyaji T., Lilly S., Masters D., Puccetti S., Schawinski K., Scov-

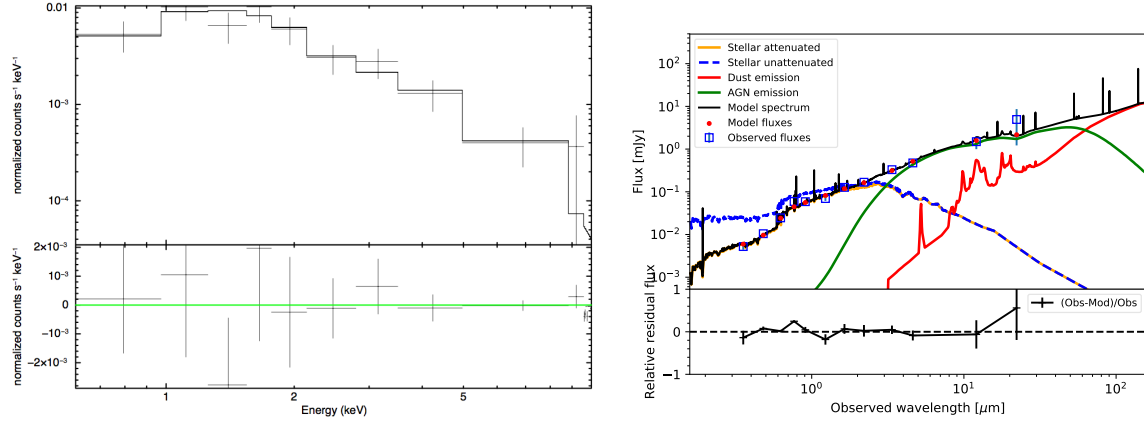


Figure 5. An example of an IR AGN at $ra = 17.55$, $dec = -0.13$, $z = 0.58$, that is X-ray absorbed ($\log(N_H/\text{cm}^{-2}) = 22.34^{+0.13}_{-0.22}$, $\Gamma = 2.12^{+0.25}_{-0.09}$), red ($r - W2 = 7.46$) and optically obscured ($\Psi = 0.001^\circ$).

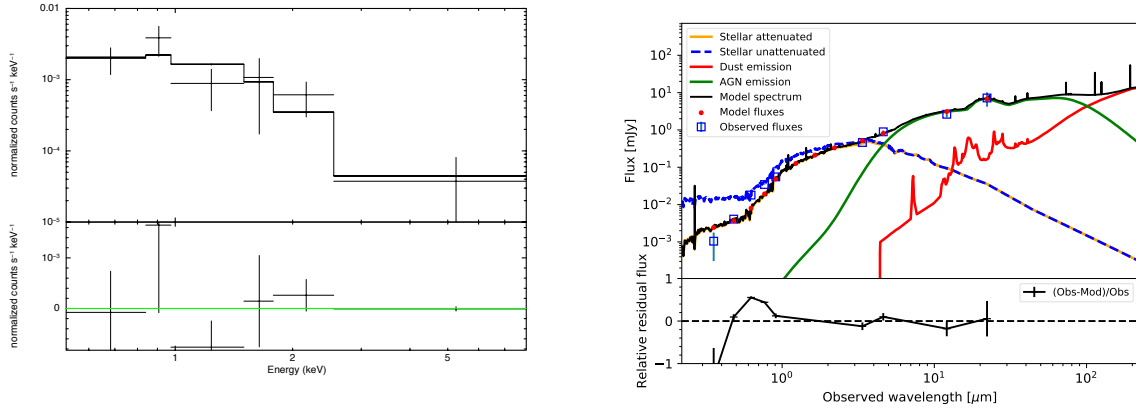


Figure 6. An example of an IR AGN at $ra = 22.75$, $dec = 0.29$, $z = 1.22$, that is X-ray unabsorbed ($\log(N_H/\text{cm}^{-2}) = 21.35^{+0.15}_{-0.06}$, $\Gamma = 1.62^{+0.13}_{-0.21}$), red ($r - W2 = 9.16$) and optically obscured ($\Psi = 0.001^\circ$).

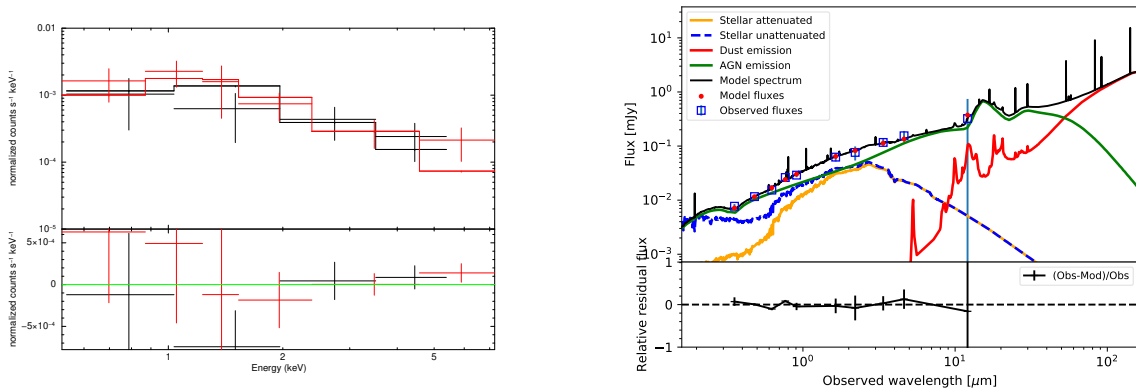


Figure 7. An example of an IR AGN at $ra = 26.57$, $dec = 0.87$, $z = 1.3$, that is X-ray unabsorbed ($\log(N_H/\text{cm}^{-2}) = 21.67^{+0.25}_{-0.19}$, $\Gamma = 1.75^{+0.17}_{-0.12}$), red ($r - W2 = 6.23$) and optically unobscured ($\Psi = 89.99^\circ$). The SED reveals that the source is a galaxy dominated system (see text for more details).

Table 4. r-W2 values and spectral fitting results of the 58 sources, that although they are optically red and obscured based on their SEDs, they do not appear X-ray absorbed.

RA	DEC	z	r-W2	Counts	$\log(N_{\text{H}}/\text{cm}^{-2})$	$-\log \Delta N_{\text{H}}$	$+\log \Delta N_{\text{H}}$	Γ	$-\Delta\Gamma$	$+\Delta\Gamma$	$\log L_{\text{X}}$ (2 – 10 keV)
22.75191	0.28993	1.215	7.55	78	21.33	0.27	0.18	1.83	0.20	0.27	44.6
14.17168	-0.39824	0.732	7.22	42	21.69	0.24	0.18	1.88	0.22	0.26	43.7
19.09421	0.12796	1.123	6.61	68	21.05	0.97	0.50	1.91	0.21	0.21	44.0
15.91209	0.39683	1.018	6.59	57	21.83	1.69	0.28	1.86	0.24	0.23	44.2
18.58634	-0.39547	2.020	6.54	71	20.28	0.19	1.82	1.92	0.24	0.17	44.9
24.64576	0.36487	0.799	6.39	21	20.65	0.59	0.85	1.91	0.25	0.23	44.2
27.06873	0.23135	2.060	6.38	55	21.27	1.04	0.26	1.99	0.30	0.16	44.8
18.53689	0.12753	0.748	6.36	36	21.25	1.14	0.37	1.83	0.20	0.29	44.1
23.47359	-0.25258	0.448	6.32	87	21.37	0.32	0.24	1.93	0.22	0.25	43.5
19.70129	-0.387586	1.498	6.26	42	21.61	0.92	0.49	1.80	0.21	0.27	44.0
15.25358	-0.39835	1.147	6.25	47	21.72	0.82	0.19	1.87	0.21	0.24	43.8
14.15460	-0.44718	0.474	6.24	252	20.12	0.10	0.64	2.02	0.18	0.15	44.3
20.25309	-0.25531	0.864	6.23	622	20.09	0.06	0.54	1.94	0.08	0.15	43.9
25.77309	0.2756	1.048	6.20	252	20.18	0.13	1.07	1.85	0.12	0.19	44.6
27.64483	-0.03117	1.739	6.14	224	20.28	0.23	0.88	2.04	0.12	0.21	44.5
23.88331	0.19228	1.152	6.11	68	20.43	0.36	1.12	1.98	0.23	0.23	44.3
25.23941	0.1812	0.523	6.08	1970	20.00	0.02	0.05	1.99	0.07	0.07	44.5
16.59543	-0.35543	0.448	6.07	82	21.69	0.70	0.36	1.93	0.25	0.21	44.2
26.54346	-0.16881	1.016	6.06	68	20.11	0.03	1.42	1.93	0.19	0.22	44.3
20.49188	1.13305	0.58	8.65	48	21.55	1.42	0.31	1.92	0.18	0.29	43.8
23.55290	0.06254	0.88	7.98	471	20.42	0.14	0.17	2.02	0.12	0.12	44.6
26.38281	-0.04591	1.03	7.88	65	20.95	0.62	0.75	1.66	0.27	0.25	44.1
22.75191	0.28993	1.19	7.55	276	21.59	0.20	0.56	1.94	0.14	0.15	44.4
25.02285	-0.55147	0.75	7.26	776	21.67	0.05	0.03	1.88	0.07	0.13	44.8
16.94573	-0.34984	0.57	7.04	56	20.92	0.84	0.25	2.12	0.21	0.28	43.8
18.86014	-0.08849	0.88	6.89	162	20.33	0.32	0.40	2.31	0.14	0.16	44.3
27.35273	-0.4=966	0.59	6.85	59	20.75	0.67	0.46	2.04	0.19	0.24	43.6
17.77068	-0.27414	0.37	6.73	1309	21.68	0.02	0.04	2.06	0.06	0.14	45.2
22.71088	-0.18812	1.35	6.70	87	21.22	1.14	0.41	1.92	0.22	0.31	43.9
19.09421	0.12796	1.12	6.61	150	20.41	0.37	0.41	1.92	0.14	0.18	44.1
13.66238	-1.18152	1.37	6.59	51	20.69	0.42	0.31	2.07	0.24	0.23	44.0
26.98311	0.22810	1.64	6.54	138	21.57	0.40	1.38	2.24	0.19	0.15	44.3
18.58251	-0.39484	2.02	6.54	92	20.64	0.48	0.25	2.01	0.24	0.25	44.1
21.37418	-1.24827	0.82	6.48	29	21.00	0.61	1.82	1.81	0.31	0.29	43.7
15.14123	0.12564	1.06	6.45	73	21.25	0.45	0.29	1.75	0.25	0.24	43.9
24.63729	0.36478	0.80	6.39	484	21.83	0.20	0.15	2.07	0.13	0.14	44.6
18.53689	0.12753	0.75	6.36	133	21.32	0.29	0.38	1.85	0.20	0.19	44.1
26.82609	-0.13351	0.54	6.36	123	21.58	0.45	0.29	2.05	0.18	0.15	44.4
16.39569	0.10205	1.30	6.32	132	20.86	0.42	1.21	1.75	0.21	0.16	44.3
27.78665	0.58813	0.88	6.31	55	20.81	0.65	0.34	2.10	0.26	0.21	43.9
19.70257	-0.38753	1.50	6.26	76	20.50	0.40	0.82	1.62	0.17	0.28	43.9
26.52557	0.32857	0.90	6.25	1083	21.69	0.04	0.02	2.15	0.05	0.12	44.6
14.15460	-0.44718	0.47	6.24	111	20.24	0.24	0.82	1.94	0.24	0.21	44.2
16.35091	0.15034	0.42	6.24	69	20.69	0.62	0.45	1.85	0.28	0.29	44.0
20.25309	-0.25531	0.86	6.23	100	21.24	0.47	0.28	1.92	0.19	0.25	44.2
18.81533	0.4096	1.94	6.19	73	21.42	0.96	0.61	1.97	0.21	0.18	43.9
16.23248	0.28018	0.72	6.13	531	21.69	0.05	0.8	2.35	0.09	0.14	44.6
22.89568	0.18808	0.90	6.12	92	21.52	0.43	0.21	2.01	0.26	0.25	44.1
18.30137	0.10406	0.97	6.11	127	21.50	0.31	0.39	1.75	0.17	0.19	44.1
16.47210	-0.01478	1.05	6.09	185	21.00	0.52	0.74	1.89	0.19	0.14	44.2
26.88057	-0.15136	2.24	6.09	127	21.82	0.32	0.24	1.92	0.16	0.18	44.0
28.26243	1.01048	1.31	6.08	57	20.91	0.52	1.91	1.95	0.27	0.21	43.8
16.59543	-0.35543	0.45	6.07	112	20.39	0.32	0.25	2.08	0.21	0.20	44.0
19.61204	-0.49189	1.16	6.07	71	21.52	1.21	0.58	1.72	0.22	0.29	43.9
27.80391	0.50809	0.70	6.04	204	20.20	0.25	1.21	1.92	0.15	0.15	44.4
26.88310	-0.33868	0.55	6.04	50	21.05	0.49	0.73	2.14	0.25	0.27	43.8
27.27786	-0.37372	1.07	6.01	225	21.30	0.18	0.27	1.83	0.16	0.14	44.5
28.77457	0.59739	1.07	6.00	168	21.69	0.34	0.51	1.99	0.14	0.18	44.3

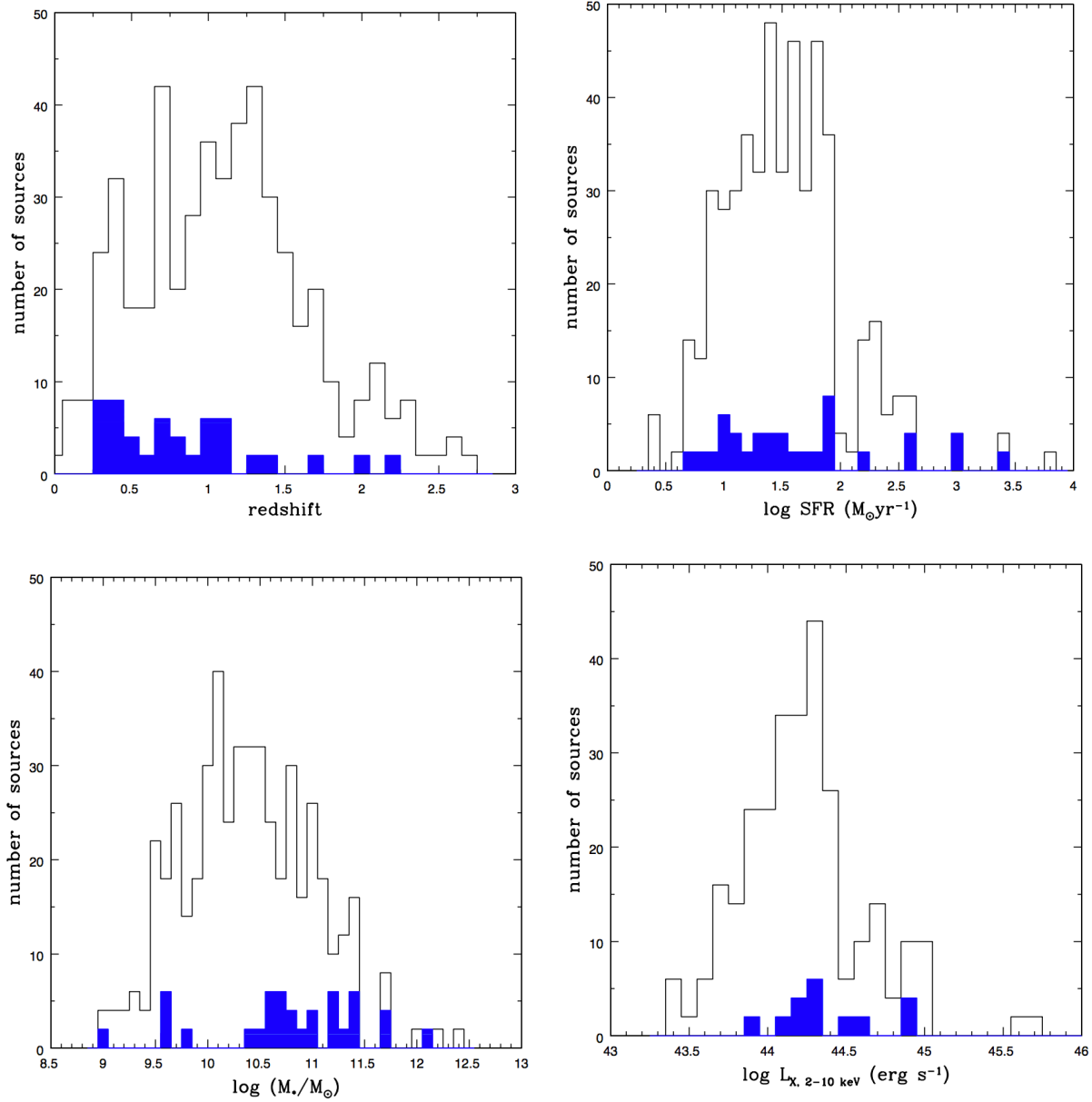


Figure 8. Redshift, SFR, stellar mass calculations (derived by SED fitting) and X-ray luminosities (derived by X-ray spectral fitting), for the total population of X-ray unabsorbed, IR AGN (black line) and for the X-ray unabsorbed, optically red and obscured sources (blue shaded regions; see text for more details). We notice that the latter population consists of luminous AGN that (the bulk of it) lives in massive systems with $\log(M_*/M_\odot) > 10.5$.

ille N. Z., Silverman J., Trump J., Urry M., Vignali C., Wright N. J., 2012, *ApJS*, 201, 30

Civano F., Hickox R. C., Puccetti S., Comastri A., Mullaney J. R., Zappacosta L., LaMassa S. M., Aird J., Alexander D. M., Ballantyne D. R., Bauer F. E., Brandt W. N., Boggs S. E., Christensen F. E., Craig W. W., Del-Moro A., Elvis M., Forster K., Gandhi P., Grefenstette B. W., Hailey C. J., Harrison F. A., Lansbury G. B., Luo B., Madsen K., Saez C., Stern D., Treister E., Urry M. C., Wik D. R., Zhang W., 2015, *The Astrophysical Journal*, 808, 185

Corral A., Georgantopoulos I., Watson M. G., Rosen S. R., Page K. L., Webb N. A., 2015, *A&A*, 576, A61

Dale D. A., Helou G., Magdis G. E., Armus L., Díaz-Santos T., Shi Y., 2014, *ApJ*, 784, 83

Dalton G. B., Caldwell M., Ward A. K., Whalley M. S., Wood-

house G., Edeson R. L., Clark P., Beard S. M., Gallie A. M., Todd S. P., Strachan J. M. D., Bezawada N. N., Sutherland W. J., Emerson J. P., 2006, *SPIE*, 6269

Del Moro A., et al., 2016, *MNRAS*, 456, 2105

Donley J. L., Koekemoer A. M., Brusa M., Capak P., Cardamone C. N., Civano F., Ilbert O., Impey C. D., Kartaltepe J. S., Miyaji T., Salvato M., Sanders D. B., Trump J. R., Zamorani G., 2012, *ApJ*, 748, 142

Eckart M. E., McGreer I. D., Stern D., Harrison F. A., Helfand D. J., 2010, *The Astrophysical Journal*, 708, 584

Emerson J., McPherson A., Sutherland W., 2006, *Msngr*, 126, 41

Feroz F., Hobson M. P., Bridges M., 2009, *MNRAS*, 398, 1601

Fiore F., Puccetti S., Brusa M., Salvato M., Zamorani G., Aldcroft T., Aussel H., Brunner H., Capak P., Cappelluti N., Civano

F., Comastri A., Elvis M., Feruglio C., Finoguenov A., Fruscione A., Gilli R., Hasinger G., Koekemoer A., Kartaltepe J., Ilbert O., Impey C., Le Floc'h E., Lilly S., Mainieri V., Martinez-Sansigre A., McCracken H. J., Menci N., Merloni A., Miyaji T., Sanders D. B., Sargent M., Schinnerer E., Scoville N., Silverman J., Smolcic V., Steffen A., Santini P., Taniguchi Y., Thompson D., Trump J. R., Vignali C., Urry M., Yan L., 2009, *ApJ*, 693, 447

Freeman P. E., Doe S., Siemiginowska A., 2001, *ASPC*, 238, 483

Fritz J., Franceschini A., Hatziminaoglou E., 2006, *MNRAS*, 166, 767

Georgantopoulos I., Georgakakis A., Rowan-Robinson M., Rovi-
los E., 2008, *A&A*, 484, 671

Glikman E., et al., 2018, *ApJ*, 861, 37

Kalberla P. M. W., Burton W. B., Hartmann D., Arnal E. M., Ba-
jaja E., Morras R., Pöppel W. G. L., 2005, *A&A*, 440, 775

LaMassa S. M., Cales S., Moran E. C., Myers A. D., Richards
G. T., Eracleous M., Heckman T. M., Gallo L., Urry C. M., 2015,
ApJ, 800, 144

LaMassa S. M., Georgakakis A., Vivek M., Salvato M., Ananna
T. T., Urry C. M., MacLeod C., Ross N., 2019, *ApJ*, 876, 50

LaMassa S. M., Urry C. M., Cappelluti N., Civano F., Ranalli P.,
Glikman E., Treister E., Richards G., Ballantyne D., Stern D.,
Comastri A., Cardamone C., Schawinski K., Böhringer H., Chon
G., Murray S. S., Green P., Nandra K., 2013, *Monthly Notices of
the Royal Astronomical Society*, 436, 3581

LaMassa S. M., et al., 2013a, *MNRAS*, 432, 135

—, 2013b, *MNRAS*, 436, 3581

Lawrence A., et al., 2007, *MNRAS*, 379, 1599

Mateos S., Alonso-Herrero A., Carrera F. J., Blain A., Watson
M. G., Barcons X., Braito V., Severgnini P., Donley J. L., Stern
D., 2012, *MNRAS*, 426, 3271

Mateos S., et al., 2017, *ApJL*, 841, 18

Mendez A. J., et al., 2013, *ApJ*, 770, 40

Mountrichas G., et al., 2017, *MNRAS*, 468, 3042

Nandra K., Pounds K. A., 1994, *MNRAS*, 268, 405

Noll S., et al., 2009, *A&A*, 507, 1793

Rosen S. R., Webb N. A., Watson M. G., Ballet J., Barret D.,
Braito V., Carrera F. J., Ceballos M. T., Coriat M., Della Ceca
R., Denkinson G., Esquej P., Farrell S. A., Freyberg M., Grisé
F., Guillout P., Heil L., Koliopanos F., Law-Green D., Lamer G.,
Lin D., Martino R., Michel L., Motch C., Nebot Gomez-Moran
A., Page C. G., Page K., Page M., Pakull M. W., Pye J., Read A.,
Rodriguez P., Sakano M., Saxton R., Schwoppe A., Scott A. E.,
Sturm R., Traulsen I., Yershov V., Zolotukhin I., 2016, *A&A*,
590, A1

Secrest N. J., Dudik R. P., Dorland B. N., Zacharias N., Makarov
V., Fey A., Frouard J., Finch C., 2015, *ApJS*, 221, 12

Stern D., Assef R. J., Benford D. J., Blain A., Cutri R., Dey A.,
Eisenhardt P., Griffith R. L., Jarrett T. H., Lake S., Masci F., Petty
S., Stanford S. A., Tsai C.-W., Wright E. L., Yan L., Harrison F.,
Madsen K., 2012, *ApJ*, 753, 30

Stern D., Eisenhardt P., Gorjian V., Kochanek C. S., Caldwell N.,
Eisenstein D., Brodwin M., Brown M. J. I., Cool R., Dey A.,
Green P., Jannuzi B. T., Murray S. S., Pahre M. A., Willner S. P.,
2005, *ApJ*, 631, 163

Viero M. P., et al., 2014, *ApJS*, 210, 9

Wright E. L., Eisenhardt P. R. M., Mainzer A. K., Ressler M. E.,
Cutri R. M., Jarrett T., Kirkpatrick J. D., Padgett D., McMillan
R. S., Skrutskie M., Stanford S. A., Cohen M., Walker R. G.,
Mather J. C., Leisawitz D., Gautier III T. N., McLean I., Ben-
ford D., Lonsdale C. J., Blain A., Mendez B., Irace W. R., Duval
V., Liu F., Royer D., Heinrichsen I., Howard J., Shannon M.,

Kendall M., Walsh A. L., Larsen M., Cardon J. G., Schick S.,
Schwalm M., Abid M., Fabinsky B., Naes L., Tsai C.-W., 2010,
AJ, 140, 1868

Yan L., et al., 2013, *AJ*, 145, 55

APPENDIX A: SED FITTING

We construct SEDs for the 507 IR AGN in our sample, with X-ray detection. For that purpose, we use multiwavelength broadband photometric data from optical (SDSS-DR13; Albareti et al. 2015), near-IR (VISTA-VIKING; Emerson et al. 2006; Dalton et al. 2006) and mid-IR (WISE; Wright et al. 2010). The SEDs are fitted using the CIGALE code version 0.12 (Code Investigating GALaxy Emission; Noll et al. 2009).

In the fitting process we use the Fritz et al. (2006) library of templates to model the AGN emission. The star-formation histories are convolved assuming the double-exponentially-decreasing (2τ -dec) model (Ciesla et al. 2015). The Bruzual & Charlot (2003) template is utilized to model the stellar population synthesis, assuming the Salpeter Initial Mass Function (IMF) and the Calzetti et al. (2000) dust extinction law. Dale et al. (2014) templates are adopted for the absorbed dust that is reemitted in the IR. Table A1 presents the models and the values for the free parameters used by CIGALE for the SED fitting of our X-ray AGN. We consider a source as type 2 when the inclination angle of the torus, Ψ , is $\Psi = 0.001^\circ$ or $\Psi = 50.10^\circ$.

Table A1. The models and the values for their free parameters used by CIGALE for the SED fitting of our X-ray AGN. τ is the e-folding time of the main stellar population model in Myr, age is the age of the main stellar population in the galaxy in Myr (the precision is 1 Myr), burst age is the age of the late burst in Myr (the precision is 1 Myr). β and γ are the parameters used to define the law for the spatial behaviour of density of the torus density. The functional form of the latter is $\rho(r, \theta) \propto r^\beta e^{-\gamma|\cos\theta|}$, where r and θ are the radial distance and the polar distance, respectively. Θ is the opening angle and Ψ the inclination angle of the torus. Type-2 AGN have $\Psi = 0.001^\circ$ and Type-1 AGN have $\Psi = 89.99^\circ$. The AGN fraction is measured as the AGN emission relative to IR luminosity ($1 - 1000 \mu m$).

Parameter	Model/values
Stellar population synthesis model	
Initial Mass Function	Salpeter
Metallicity	0.02 (Solar)
Single Stellar Population Library	Bruzual & Charlot (2003)
double-exponentially-decreasing (2τ -dec) model	
τ	100, 1000, 5000, 10000
age	500, 2000, 5000, 10000, 12000
burst age	100, 200, 400
Dust extinction	
Dust attenuation law	Calzetti et al. (2000)
Reddening E(B-V)	0.3
E(B-V) reduction factor between old and young stellar population	0.44
Fritz et al. (2006) model for AGN emission	
Ratio between outer and inner dust torus radii	60
$9.7 \mu m$ equatorial optical depth	0.1, 0.3, 1.0, 2.0, 6.0, 10.0
β	-1.00, -0.5, 0.00
γ	0.0, 2.0, 6.0
Θ	100
Ψ	0.001, 50.10, 89.99
AGN fraction	0.1, 0.2, 0.3, 0.5, 0.6, 0.8